

GRADED ORBITAL OCCUPATION NEAR INTERFACES IN A $\text{La}_2\text{NiO}_4 - \text{La}_2\text{CuO}_4$ SUPERLATTICE

S. Smadici,¹ J. C. T. Lee,¹ J. Morales,¹ G. Logvenov,^{2,*} O. Pelleg,² I. Bozovic,² Y. Zhu,² and P. Abbamonte¹

¹*Frederick Seitz Materials Research Laboratory, University of Illinois, Urbana, IL 61801, USA*

²*Brookhaven National Laboratory, Upton, NY 11973, USA*

X-ray absorption spectroscopy and resonant soft x-ray reflectivity show a non-uniform distribution of oxygen holes in a $\text{La}_2\text{NiO}_4 - \text{La}_2\text{CuO}_4$ (LNO-LCO) superlattice, with excess holes concentrated in the LNO layers. Weak ferromagnetism with $T_c = 160$ K suggests a coordinated tilting of NiO_6 octahedra, similar to that of bulk LNO. Ni $d_{3z^2-r^2}$ orbitals within the LNO layers have a spatially variable occupation. This variation of the Ni valence near LNO-LCO interfaces is observed with resonant soft x-ray reflectivity at the Ni and Cu L edges, at a reflection suppressed by the symmetry of the structure, and is possible through graded doping with holes, due to oxygen interstitials taken up preferentially by inner LNO layers. Since the density of oxygen atoms in the structure can be smoothly varied with standard procedures, this orbital occupation, robust up to at least 280 K, is tunable.

I. INTRODUCTION

Orbital states of transition metal (TM) oxides present the opportunity of adjusting material properties to a specific purpose. In practice, spin and orbital reconstructions by charge transfer have been observed near the LCMO-YBCO interfaces^{1,2}, which locally have the structure of 113 oxides between Cu and Mn atomic planes. Other layered structures have been proposed, where strain, electronic confinement or correlations remove the bulk orbital degeneracy³, leaving only one orbital available for transport, similar to the Cu $d_{x^2-y^2}$ orbital in high-temperature superconductors. The $\text{LaNiO}_3 - \text{LaAlO}_3$ superlattices³⁻⁶ where the degeneracy of the e_g orbitals in LaNiO_3 is removed, is an example of using these ideas for orbital reconstruction and control of correlated phases of TM oxides with the 113 structure.

It is intriguing to ask whether these ideas can be extended to 214 materials. In some bulk 113 structures (e.g. SrTiO_3) the TM ion moves away from the center of the oxygen octahedron and the orbital degeneracy is lifted by the crystal-field splitting. Strain can determine the relative order of thin film 113 e_g orbitals if the orbitals are degenerate in the bulk.⁷ For instance, when the apical oxygen atoms are moved farther along the c -axis, the $d_{3z^2-r^2}$ orbital becomes lower in energy than the $d_{x^2-y^2}$ orbital. For TM ions compounds with the 214 structure, the degeneracy of e_g orbitals is similarly lifted by the crystal-field splitting. In this case, the order of e_g orbitals is not modified by strain because the orbital energy change associated with it (~ 0.1 eV) is relatively small compared to the crystal-field splitting (~ 1 eV). In addition, in contrast to 113 structures, additional atomic layers are present between TM layers in 214 compounds. This raises the question of whether 214 heterostructure interfaces will affect the occupation of TM orbitals away from bulk properties sufficiently strongly, through confinement effects, charge transfer or in other ways.

Here, we investigate the effect of interfaces on oxygen dopant distribution and TM orbital occupations in a su-

perlattice made of La_2NiO_4 (LNO) and La_2CuO_4 (LCO) layers. We observed that oxygen atoms are doping preferentially the LNO layers, changing the TM orbital occupation. More importantly, they can allow a reflection suppressed by symmetry, with the dopant-induced scattering separated in momentum from other charge scattering. A spatially variable Ni valence and d -orbital occupation within the LNO layers is observed in this way with resonant soft x-ray scattering. We therefore found that superlattice interfaces can significantly affect the occupation of the TM orbitals in 214 oxides.

This corroborates the observation that oxygen content can determine the transport properties of 113 TM oxide heterostructures. For instance, LaAlO_3 films on SrTiO_3 (STO) substrates are insulating or metallic, depending on the number of oxygen vacancies.⁸ Our results show that, to understand the properties of oxide heterostructures, it might be necessary to consider the oxygen dopant distribution, not only the average content. Since the oxygen interstitial distribution is relatively easily modified with standard procedures, this orbital occupation in 214 LNO-LCO superlattices is tunable.

II. EXPERIMENTS

A. Superlattice structure

The superlattice, made of LNO and LCO layers on a STO substrate, was grown by molecular beam epitaxy at Brookhaven National Laboratory. Atomic force microscopy (AFM) measurements on a Dimension 3100 instrument showed good superlattice surface quality with an average rms roughness over a $5 \mu\text{m} \times 5 \mu\text{m}$ area of 0.53 nm. The sample has La in both layers; therefore it is not possible to use scattering near the La edge to characterize the interface roughness.⁹

Off-specular hard x-ray scattering measurements (not shown) confirmed that the superlattice is fully strained in the $a - b$ plane to the STO substrate with $a_s = b_s =$

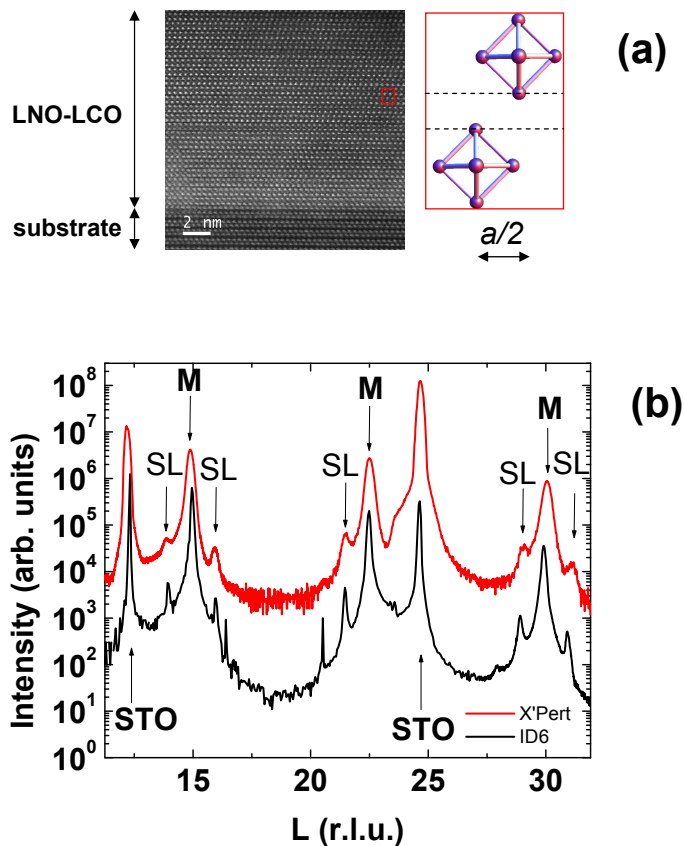


FIG. 1: (color online) (a) STEM high angle annular dark field image of a LNO-LCO superlattice showing epitaxial growth. The right panel expands the image area enclosed by the rectangle. The bright features in the image are La atoms in the LaO planes, represented by dashed lines between the TM–O₆ octahedra. The oxygen atoms are not visible. The experimental conditions were 1.3 Å probe size at 200 kV, 28 mrad convergence angle, and 64 – 341 mrad collection angle. (b) Wide angle hard x-ray measurements made at Advanced Photon Source at Argonne National Laboratory (7.5 keV) and with an X’ Pert diffractometer (8.05 keV) showing superlattice peaks (SL) near the main reflections (M) indexed with respect to the measured superperiod. Substrate peaks (STO) are also visible.

3.915 ± 0.035 Å. A comparison to measurements on bulk LNO and LCO single crystals^{10,11} indicates that the LNO layers are under tensile stresses of 1.5 % and 0.6 % along the a and b directions of the STO substrate, while the LCO layers are under tensile stresses of 3.4 % and 2.7 % along the a and b directions.

Hard x-ray reflectivity (HXR) scans (Fig. 1b), made at beamline ID6 at the Advanced Photon Source at Argonne National Laboratory and using a laboratory X’Pert x-ray source, showed pronounced superlattice peaks. The average monolayer thickness was 6.470 ± 0.035 Å, defined as 1 “molecular layer” (ML), and corresponding to half the average of LNO and LCO unit cells c -axis parameters. The number of ML in a superperiod was determined by measuring the ratio of momentum transfers for superlat-

tice reflections satellites (SL) to momentum transfers of Bragg peaks (M in Fig. 1b) corresponding to 1 ML. The average of ID6 and X’Pert measurements showed a superlattice period of (7.45 ± 0.08) ML and (7.42 ± 0.14) ML, respectively, indicating an approximately equal mixture of 7 ML and 8 ML superperiods.

The average ML thickness, number of MLs in a superperiod and number of superperiods (12 deposition repeats), give a total superlattice thickness of 577 ± 10 Å, consistent with the result obtained from thickness oscillations (Fig. 2) of 570 ± 20 Å.

The superlattice deposition sequence had LNO and LCO layers of nominally equal thicknesses. Indeed, HXR measurements showed a step-like feature at $L = 2$, with the scattering momentum $Q = 2\pi L/c$ indexed with respect to the superlattice superperiod c for low- Q range, on a large sloping background (ID6 curve in Fig. 2). This arises from the slightly different c -axis parameters of LNO and LCO unit cells. Scattering at the $L = 2$ superlattice reflection is suppressed for equal LNO and LCO layer thicknesses. Thus, the thicknesses of the LNO and LCO layers will be considered equal in the following analysis. However, the $L = 2$ peak, suppressed for non-resonant HXR scattering, is observed for resonant x-ray scattering at the Ni edge, but not at the Cu edge. This, *regardless of any irregularities of the structure*, highlights a difference in the initial and intermediate state distributions of resonant scattering at the Ni edge, that is a difference between the distributions of atomic cores and Ni valence electronic states. In Section II.E, it will be shown how this can happen at the Ni edge (Fig. 2).

B. Superlattice magnetism

Undoped bulk LNO and LCO are antiferromagnetic insulators with two and one unoccupied TM orbitals and nominal $S = 1$ and $S = 1/2$ spins on the Ni²⁺ and Cu²⁺ ions, respectively. Bulk La₂NiO_{4.03} shows a weak ferromagnetism below 65 K with a net magnetic moment oriented along the c -axis of approximately $0.04 \mu_B/\text{Ni}$ ion at 4.2 K.¹² The ferromagnetism is not the consequence of oxygen doping; the NiO₆ octahedra in undoped bulk LNO tilt in the low-temperature tetragonal phase, misaligning the spins and making the material weakly ferromagnetic.¹³ In doped LNO the ferromagnetic phase appears below $\sim 150 - 200$ K.¹³

SQUID measurements of the superlattice, done with a Quantum Design instrument, showed a ferromagnetic moment below $T = 160$ K (Fig. 3), with $\lesssim 0.05 \mu_B/(\text{Ni ion})$, consistent with the magnitude of bulk LNO ferromagnetism. The SQUID measurements also did not show a superconducting anomaly in the magnetic moment down to 10 K, which sets an upper limit on hole doping of the LCO layers of 0.06.¹⁴

The consistency of the magnitude of the moment and temperature of the transition with that of bulk LNO suggest that the superlattice ferromagnetism is likely con-

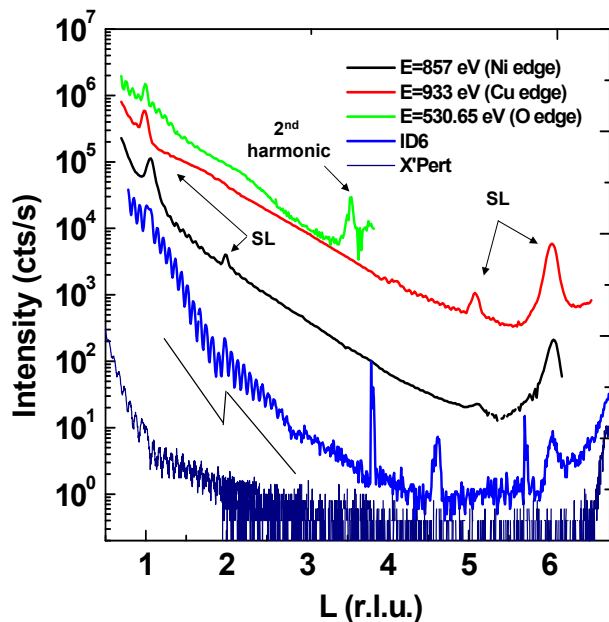


FIG. 2: (color online) L scans of the low momentum range for hard and soft x-ray scattering. HXR measurements show strong thickness oscillations, with a peak at $L = 1$ and a step at $L = 2$ (black line) for ID6 data. The peaks at $L=3.8$, 4.6, and 5.7 are stray reflections. Soft x-ray scattering shows pronounced superlattice (SL) peaks for $L = 1$ at O K, Ni L and Cu L edges. The Ni $L = 1$ peak is shifted because of refraction. The $L=2$ reflection is much larger at the Ni edge compared to the Cu edge. This observation is confirmed by detailed energy-resolved measurements (Fig. 6) which are discussed below. In contrast, the absence of the $L=2$ reflection in measurements at the oxygen edge is caused by the energy used (see Fig. 5 for a complete measurement). Smaller differences can be observed between the measurements at the Cu and Ni edges, for instance a slight indication of a peak at $L = 4$ at the Cu edge. The small difference in intensity at $L = 4$ can be explained using the different polarizations of Ni and Cu d -orbitals, unlike the opposite and larger difference at $L = 2$ (Sec. II E). The intensity of SL reflections at $L = 3$ and $L = 4$ is small, consistent with the calculated dependence of SL structure factors amplitude on L . The $L = 5$ and $L = 6$ SL peaks are larger because of the proximity to the Bragg peak corresponding to 1 ML (off x -axis in this figure).

finer to the LNO layers, where the magnetic moment has a similar origin to that of bulk LNO. The necessary corresponding modifications to the magnitude of Ni spins near the interfaces from different Ni orbital occupations, discussed later and shown schematically in Fig. 8b, do not appear to result in large additional ferromagnetic moments. In this case, this is likely because exchange correlations decay spatially very fast and the net magnetic moment of NiO_2 and CuO_2 layers in bulk compounds is small or zero, respectively. The temperature variation of the SL ferromagnetism will invalidate a candidate explanation for the difference at $L=2$ in the resonant soft x-ray scattering at the Ni and the Cu edges (Sec. II E). We will use the smallness of the superlattice ferromagnetic

moment in Section III.A.

C. Hole distribution

Oxygen doping bulk LNO and LCO places oxygen interstitials between the LaO layers of the structure.¹⁵ The electronic structures and orbital orientations of bulk LNO and LCO, studied with x-ray absorption spectroscopy (XAS) experiments on bulk nickelates^{13,16,17} and cuprates¹⁸, showed doping-dependent upper Hubbard bands (UHB) and mobile carrier peaks (MCP).

XAS measurements showed a non-uniform distribution of holes in the SL and the favorable conditions for a large Ni valence modulation. We used XAS in total fluorescence yield (TFY) and total electron yield (TEY) modes to characterize the hole distribution in the LNO-LCO superlattice (Fig. 4a). Measurements were made at beamline X1B at the National Synchrotron Light Source at Brookhaven National Laboratory. To determine which peak belongs to which layer, the short probing depth of TEY compared to TFY was used to isolate the signal from the shallower layer of the superperiod, which is known from the deposition sequence to be LNO. For energies in the range of a few hundred eV, as in our case, the TEY probing depth is less than 100 Å. In contrast, the penetration depth of TFY at these energies is thousands of Å, effectively probing the entire superlattice. Therefore, the peaks that are present in TFY but not TEY originate from the deeper layer of the superperiod pair, which is the LCO layer.

Fig. 4a shows TFY and TEY measurements on the superlattice at room temperature. The lowest energy peak that originates in the LCO layers aligns with the upper-Hubbard band (UHB) peak of bulk LCO,¹⁸ while the lowest-energy peak in the LNO layers aligns with the mobile carrier peak (MCP) of bulk LNO.^{16,17} This suggests that the LCO layers of the superlattice are undoped, consistent with the magnetization measurements in Section II.B, while the LNO layers are doped by excess oxygen. The LCO MCP peak begins to be clearly present at $x \sim 0.03$ in bulk $\text{La}_{2-x}\text{Sr}_x\text{CuO}_4$ ¹⁸; since no such peak is visible for the LNO-LCO superlattice, it must be that $x_{\text{LCO}} < 0.03$. Similarly, the LNO UHB is present up to $x \sim 0.2$ in bulk $\text{La}_{2-x}\text{Sr}_x\text{NiO}_4$ ¹⁶; since no peak is seen in TFY or scattering other than LCO UHB in this energy range, $x_{\text{LNO}} > 0.2$ or oxygen doping $\delta > 10\%$. We conclude that the doped holes are localized in the LNO layers of the superlattice.

Even with a large number of holes in the LNO layers, the superlattice remains insulating (Fig. 3). Assuming that holes are shared equally between Ni and O atoms, $x_{\text{LNO}} > 0.2$ implies that the average Ni valence increases from 2+ in undoped LNO to larger than 2.1+ in oxygen-doped LNO. It can, in principle, accommodate a substantial modulation of the Ni valence within the LNO layers. This modulation is observed by scattering at the Ni edge (Section II.E).

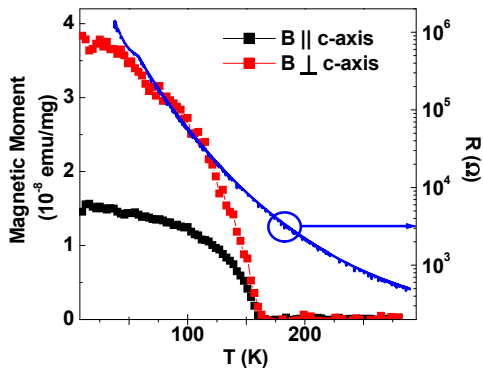


FIG. 3: (color online) Magnetic moment measurements show a ferromagnetic transition at 160 K. A diamagnetic contribution has been subtracted from the data. The applied magnetic field was 100 Oe. Resistivity measurements show an insulating behavior down to 38 K with a small anomaly in slope at 58 K.

D. Scattering at the oxygen edge

Resonant soft x-ray scattering (RSXS) can probe bulk charge order.^{19–22} Its energy and momentum selectivity makes it a useful technique for also probing the spatial distributions of orbitals of different energies in nanometer-sized structures. Measurements on the LNO-LCO superlattice at the oxygen K, Ni and Cu L edges (see Fig. 2 for selected resonant energies) were made at beamline X1B at the National Synchrotron Light Source in an ultra-high vacuum diffractometer with a π -polarized incident beam. Scattering measurements were made at 90 K, unless specified otherwise. The beam was focused to an approximately 1 mm \times 1 mm spot, which is much smaller than the sample size.

RSXS at the oxygen K edge probes the spatial distribution of the occupation of oxygen p -states and illustrates one reason for the L dependence of resonant intensities of SL reflections. Measurements were made in specular geometry with a variable energy E and momentum perpendicular to the surface $Q = 2\pi L/c$, with reflections indexed with respect to the superperiod c for low- Q range (for other examples of RSXS on superlattices, see 9,23). Figs. 4b and 5 show reflectivity measurements at the oxygen edge for $L=1$ and $L=2$, respectively. Refraction effects and small superlattice imperfections slightly shift the peaks from integer values. Peaks at 529 eV and 531.5 eV are visible for the momentum held fixed at $L=1$ (Fig. 4b), indicating a spatial modulation of the same LNO MCP and LCO UHB states that are visible at 528.5 eV and 530.5 eV in FY measurements (Fig. 4a). A third peak is present for $L=2$ at 533.5 eV (Fig. 5); this peak will be addressed in Section III.B. The ratio of the scattering intensities for LNO MCP and LCO UHB energies is different for $L=1$ and $L=2$. Specifically, $I_{\text{LNO,MCP}}/I_{\text{LCO,UHB}} = 1.1$ for $L=1$ and 0.4 for $L=2$.

The intensity of a superlattice reflection in the single-scattering approximation is given by $I = A|\hat{\epsilon}_f^* S_L \hat{\epsilon}_i|^2$,

where

$$S_L^{ij} = \sum_{l,n} \langle t_l^n \rangle f_n^{ij}(\omega) e^{i2\pi L z_l/c} \quad (1)$$

is the structure factor, $\langle t_l^n \rangle$ is the average over a layer of the occupation factor t_l^n (equal to 0 or 1), which identifies the valence and element n to use in Eq. 1 for each site in layer z_l (e.g. Ni^{2+} or Ni^{3+}), and $f_n^{ij}(\omega)$ is the atomic form factor for valence and element n , with the indices i and j accounting for X-ray birefringence. Defining the variables $\{t_l^n\}$ in Eq. 1 separates the spatial (l) and energy (ω) dependence of the scattering factor. This is justified by the very weak dependence of atomic form factors on momentum for soft x-ray energies. In comparing the intensities of LNO MCP and LCO UHB features, we neglect self-absorption effects and the change with geometry of A (e.g., footprint effects) since the scattering geometries and energies are very close. The variation with L of the intensity ratio $I_{\text{LNO,MCP}}/I_{\text{LCO,UHB}}$ can, in principle, be due to either the polarization dependence of the form factors f_n^{ij} or the spatial distribution of the occupation factors t_l^n .

Bulk LCO has hole orbitals oriented in the $a-b$ plane¹⁸, while the holes in bulk LNO have a substantial component oriented along the c -axis^{17,24,27}. The variation of the intensity ratio $I_{\text{LNO,MCP}}/I_{\text{LCO,UHB}}$ with L can be qualitatively explained by assuming a polarization of hole orbitals in the superlattice LCO and LNO layers that resembles that of bulk LCO and LNO. Specifically, the scattering intensity of a horizontally-polarized beam off intermediate states oriented along $a-b$ and c -axis is proportional to $\sin^4(\theta)$ and $\cos^4(\theta)$ respectively, where θ is the angle between the incident beam direction and the sample surface. The intensity for the LCO state will be proportional to $\sin^4(\theta)$. In contrast, for the LNO intermediate state, with a substantial component oriented along c -axis, the scattering intensity has a term proportional to $\cos^4(\theta)$ and can be expected to increase slower or even decrease as θ , and therefore L , increases. Then, to explain the variation with L of $I_{\text{LNO,MCP}}/I_{\text{LCO,UHB}}$ observed in the measurements, it is sufficient to assume, based on the relatively small influence of strain in 214 structures (Section I), that the hole p -orbital orientations in LNO and LCO layers are similar to those in bulk crystals.

The oxygen p orbitals hybridize with the TM orbitals inside the TM – O_6 octahedra (Fig. 1a). Therefore, the polarization of the oxygen form factors f^{ij} is related to that of TM form factors and a similar variation of the scattering intensity with L at the TM edges is expected. However, in contrast to the case of oxygen edge LNO MCP and LCO UHB states, in the next section it will be shown that the evolution with L of the scattering intensities for Ni and Cu orbitals cannot be explained with polarization of form factors alone.

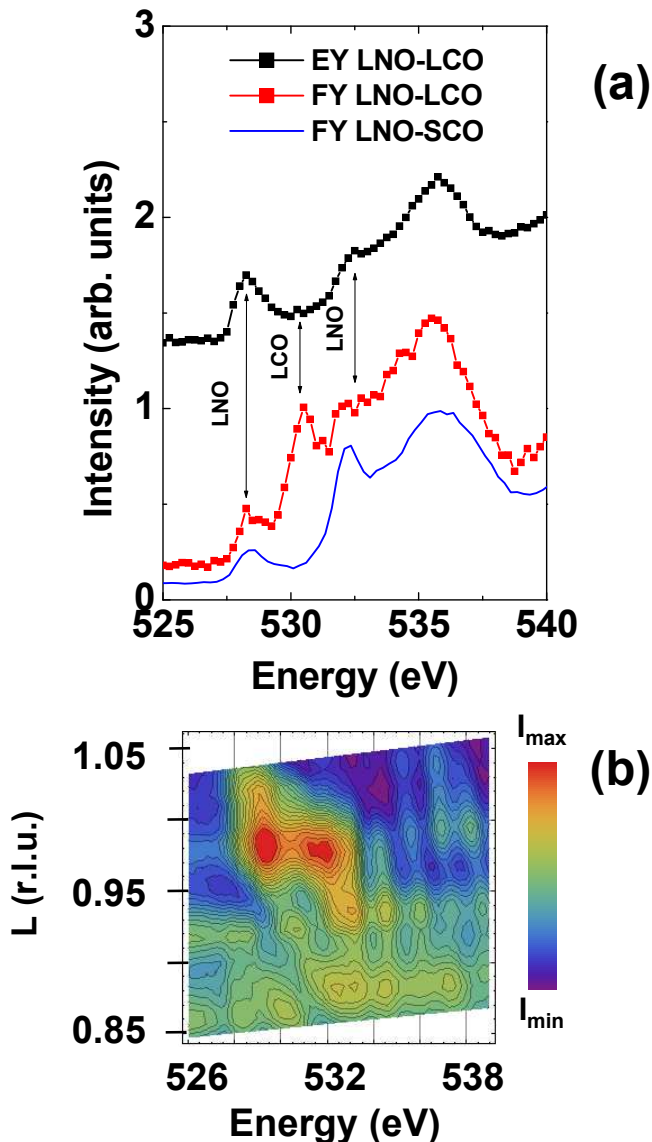


FIG. 4: (color online) (a) Electron and fluorescence yield and the correspondence of the peaks to the superlattice layers. The LCO UHB peak disappeared completely for an LNO-SCO superlattice grown on an STO substrate, showing that there is no STO substrate or LNO layer contribution at the LCO UHB energy. From detailed measurements (not shown) on LNO-SCO superlattices LNO MCP and LCO MCP have different energies. (b) RSXS intensity (logarithmic scale) at 90 K at the O edge shows two peaks corresponding to the first two peaks in TFY, with the lower (529 eV) and higher (531.5 eV) energy peaks from the LNO and LCO layers, respectively. The different L profiles are due to an interference effect and different layer c -axis parameters.

E. Scattering at transition metal edges

Resonant scattering at TM edges probes the d -states of Cu and Ni ions. L scans on resonance at these energies (Fig. 2) show the expected peaks at $L=1$. The $L=2$ peak is not visible at the Cu L edge in Fig. 2;

however, the $L=2$ peak is unexpectedly pronounced at the Ni edge. Detailed energy plots of this momentum region, shown in Fig. 6, confirm the large difference $I(L=2)/I(L=1)|_{\text{Ni}} \gg I(L=2)/I(L=1)|_{\text{Cu}}$ between the $L=2$ reflections at the two edges: the peak at the Ni edge is 100 % more intense than the background, compared to only 6 % at the Cu edge. This superlattice reflection was observed for sample azimuthal orientations with incident beam polarization at 45° and along the tetragonal $a-b$ axes (Fig. 7a). In contrast to the temperature dependence of the magnetic moment in Fig. 3, the intensity of the $L=2$ peak at the Ni edge does not change with temperature between 90 K and 280 K (Fig. 7b). Therefore, this peak is not related to ferromagnetism.

Contrast the observation of the larger $L=2$ intensity at the Ni edge compared to the Cu edge with the *opposite* trend at the O edge for LNO MCP and LCO UHB states, in which the LNO state intensity is suppressed at larger L . Therefore, the difference in the intensity ratio $I(L=2)/I(L=1)|_{\text{Ni,Cu}}$ for scattering at Ni and Cu edges cannot be explained using the difference in the orientation of p -states in the LNO and LCO layers, noted at the oxygen edge and a similar polarization of d -state TM orbitals hybridized with oxygen orbitals in their respective layers. The polarization of the form factor $f_n^{ij}(\omega)$ cannot be the explanation; instead we must look to a difference in the occupation factors t_i^n for Ni and Cu d -orbitals.

This difference originates in the different dependence of the Ni and Cu valence on doping. LNO resembles a Mott-Hubbard insulator more than LCO.²⁵ This is visible in the small degree of contrast in TFY at the Cu edge with doping of bulk LCO²⁶ and the large contrast at the Ni edge with doping bulk LNO²⁷. Therefore, the Ni d -orbitals participate in the hole doping process more than the Cu d -orbitals. The Cu d -states occupation factor t_i^n follows the distribution of the Cu ions because their valence remains close to Cu^{2+} . In contrast, the substantial oxygen doping in the LNO layers (Section II.C) and the strong coupling between hole doping and Ni d -states, empties additional Ni orbitals, thus raising the Ni ion valence toward Ni^{3+} .

Therefore, unlike the Cu case where oxygen doping is absent, the spatial distributions of both Ni atoms *and* oxygen interstitials determine the occupation of Ni d -states that is, the magnitude of t_i^n . If the oxygen dopants are not uniformly distributed within the LNO layers, a variable Ni valence results, i.e. spatial distributions t_i^n for the doped orbitals different from those of the Ni ions. In this case, as pointed out in Section II.A, since the intermediate d -states do not follow the distribution of the underlying structure represented by the core atoms, the scattering at $L=2$ is not suppressed. In the next section, we will use this observation and Eq. 1 to determine the orbital occupancies t_i^n in the LNO layers.

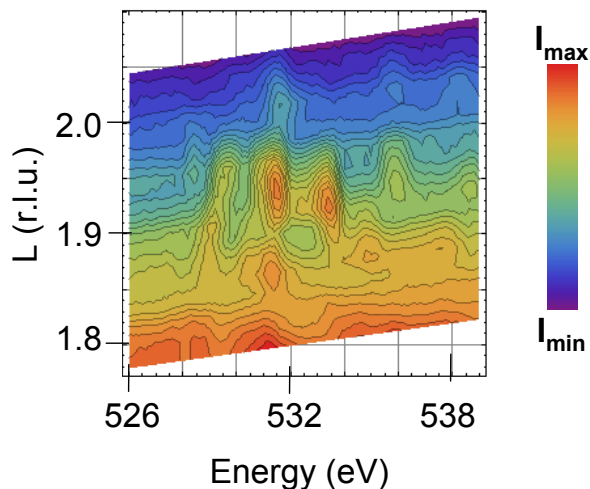


FIG. 5: (color online) Intensity of the $L=2$ reflection at the O edge at 90 K (logarithmic scale). The three peaks are (in order of increasing energy): LNO holes at $E=529.5$ eV, LCO UHB holes at $E=531.5$ eV and a feature at $E=533.5$ eV, discussed briefly in Section III.B. Unlike the scattering at $L=1$, the LNO MCP peak has substantially smaller intensity than the LCO UHB peak.

III. DISCUSSION

Our main finding does not depend on structural irregularities. The distributions of Cu and Ni atoms, and therefore of core p -states, are complementary (the layer occupations are $\langle t_l^{Cu} \rangle + \langle t_l^{Ni} \rangle = 1$, for each layer l , where $\langle t \rangle$ is the occupation factor from Eq. 1), as supported by the observation of a crystalline SL structure with Cu and Ni atoms occupying their normal sites within the 214 unit cell. Complementary distributions have the same absolute value of the Fourier transform amplitude at $L=2$. Therefore, if one does not consider differences in the Cu and Ni d -state occupations, since the core p -states (the initial states of the RSXS transition) distributions are complementary, for any value of superlattice superperiod, specific model of the distribution of interface atoms (not necessarily Gaussian as we assume in Sec. III B) or size of interface roughness, the $L=2$ peak cannot be suppressed at the Cu edge without being also suppressed at the Ni edge. To explain the difference in scattering at $L=2$, it is necessary to consider differences in the d -states (the intermediate states of the RSXS transition) that is, in the electronic properties of the LCO and LNO layers.

The difference in the $L=2$ scattering at the Cu and Ni edges cannot be attributed to a different resonant form factor $f^{ij}(\omega)$ for the Cu and Ni edges. The energy ω and momentum L variables are separable in the soft X-ray scattering cross-section (Eq. 1); therefore, since Cu and Ni atoms scatter at $L=1$, considering only the different form factors $f^{ij}(\omega)$ will imply that both scatter at $L=2$, contrary to observations.

The conclusion that the Ni valence is not constant in the LNO layers is obtained from comparing the presence

of $L=2$ scattering at the Ni edge with its absence at the Cu edge in the scattering model of Sec. III A. The measured ratio $I(L=2)/I(L=1)$ at the Ni edge and use of specific SL structure models are necessary for a quantitative estimate (Sec. III B).

A. Scattering model

Calculating the energy dependence of Ni edge scattering requires a knowledge of the energy and doping dependence of the scattering factors $f_l^{ij, Ni}(\omega)$ in the LNO crystalline lattice. Band structure calculations of the Ni density of states variation with doping with LSDA+U models²⁸ cannot reproduce the XAS experiments in the low-doping range²⁷. A detailed cluster analysis of energy levels of Ni^{2+} and Ni^{3+} ions in an octahedral crystal field shows that the degeneracy of the x-ray transitions is lifted, which results in a very complex transition spectrum.²⁹ This is visible in Fig. 8a (top) for Ni^{2+} and Ni^{3+} ions in a cubic field. The scattering at $L=2$ at the Ni L_3 and L_2 edges is nevertheless made of only one peak (Figs. 7c inset and 8a). This suggests that a simplified scattering model is warranted.

The scattering at the Ni edge can be analyzed using Eq. 1 and a simplified model. We define the functions $f_n^{ij}(\omega)$ first. The XAS and $L=2$ scattering energy profile (Fig. 8a) do not resemble the density of states of the intermediate unoccupied Ni d -states; for instance, each of the two peaks in the XAS at the Ni L_3 edge, following immediately after the La edge at 853.5 eV in Fig. 8a, has both $x^2 - y^2$ and $3z^2 - r^2$ character.²⁷ However, the state into which the electron is excited in the transition is well-defined and will be used as a label. Therefore, the transitions at the Ni L_3 edge are labeled by the intermediate d -states involved in the 2-step RSXS process and organized into four main groups based on the spin of this intermediate state (up or down) and its orbital symmetry ($d_{3z^2-r^2}$ and $d_{x^2-y^2}$). For undoped LNO (or a Ni^{2+} valence), two of these states are unoccupied ($d_{3z^2-r^2, \uparrow}$ and $d_{x^2-y^2, \uparrow}$). Doping toward a Ni^{3+} valence is a complex process that cannot be represented as sequential emptying of additional orbital levels. However, because of the isotropic nature of the holes in bulk LNO^{17,24}, it is expected that both the other two d -states ($d_{3z^2-r^2, \downarrow}$ and $d_{x^2-y^2, \downarrow}$) will be emptied. Indeed, polarization-dependent measurements of bulk LNO at the Ni edge show that these states are approximately equally emptied for $0 < x < 0.12$ ²⁷, becoming available for the scattering process. As at the oxygen edge, it is assumed that the bulk f^{ij} can be used for the layers of the LNO-LCO superlattice since, as pointed out in Section I, strain will not change the relative order of d -orbital energies in compounds with the 214 structure. Therefore, the atomic form factors for Ni ions in the layers are:

$$f_{2+}^{ii}(\omega) = f_{d_{3z^2-r^2, \uparrow}}^{ii} + f_{d_{x^2-y^2, \uparrow}}^{ii}, \quad (2)$$

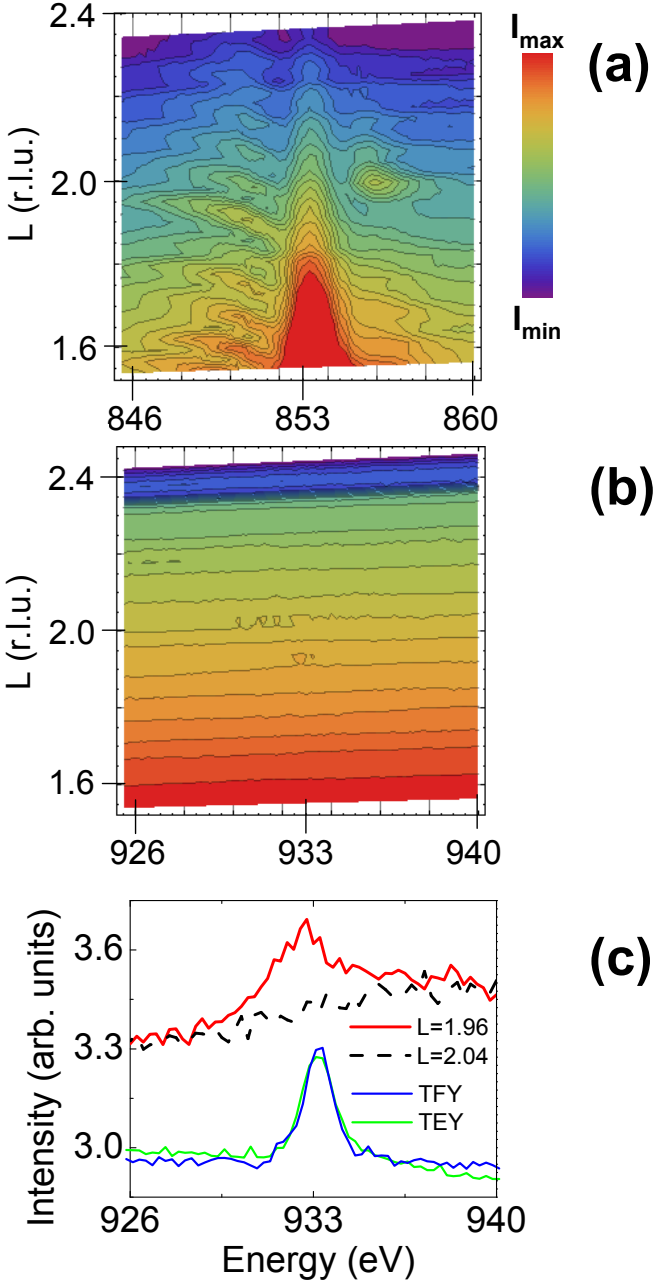


FIG. 6: (color online) (a) Scattering intensity (logarithmic scale) at La M_4 ($E=853.25$ eV) and Ni L_3 ($E=856$ eV) edges at $L=2$. The increase in the intensity over background at the Ni edge is 100 %. The features below 853 eV are thickness oscillations. No off-resonant intensity tail is observed near $L = 2$ at the Ni edge, showing that this reflection originates in an electronic state and not from, for instance, selective removal of Ni ions from the LNO layers. (b) Scattering intensity (logarithmic scale) over a wide range at the Cu edge near $L = 2$ for comparison. The energy range (14 eV) is chosen the same as in (a). (c) The area of interest at the Cu edge magnified, compared to TFY and TEY. A very small peak is visible for $L=1.96$, with a relative change in intensity over background of only 6 %. Because of the large sloping background an L scan is less useful in showing this small peak.

and

$$f_{(2+)\rightarrow(3+)}^{ii} = \frac{f_{d_{3z^2-r^2},\downarrow}^{ii} + f_{d_{x^2-y^2},\downarrow}^{ii}}{2}, \quad (3)$$

where $f_{2+}^{ij}(\omega)$ is the form factor for Ni^{2+} ions, $f_{(2+)\rightarrow(3+)}^{ij}(\omega)$ is the term added with increasing the Ni valence to Ni^{3+} , and the off-diagonal terms have been neglected because the ferromagnetic moment is small (Section II.B). These equations reflect the observation that in undoped LNO the $d_{3z^2-r^2}, \uparrow$ and $d_{x^2-y^2}, \uparrow$ levels are empty and that doping empties in approximately equal amounts the orbitals of the opposite spin.

The other term in Eq. 1 is $\langle t_l^n \rangle$. To model the momentum dependence of scattering through the orbital occupancies t_l^n , we introduce the variables p_l^{3+} and $p_l^{2+} = s_l - p_l^{3+}$, representing the layer-resolved average number of Ni atoms with nominal Ni^{3+} and Ni^{2+} valences in 1 ML over a $a_s \times b_s$ area, where s_l is the distribution of Ni ion cores. For instance, the probability that the Ni ions have the nominal Ni^{3+} valence is represented by $0 \leq p_l^{3+} \leq s_l$. From Eq. 3, the $d_{3z^2-r^2}, \downarrow$ and $d_{x^2-y^2}, \downarrow$ levels are unoccupied with a distribution following that of p_l^{3+} . Thus, the average over each layer of the occupation factors t_l^n for Ni ions are $\langle t_l^{d_{3z^2-r^2}, \uparrow} \rangle = s_l$, $\langle t_l^{d_{x^2-y^2}, \uparrow} \rangle = s_l$, $\langle t_l^{d_{3z^2-r^2}, \downarrow} \rangle = p_l^{3+}$ and $\langle t_l^{d_{x^2-y^2}, \downarrow} \rangle = p_l^{3+}$.

Then, the average Ni scattering factor in layer l depends on the variable number of unoccupied orbitals as:

$$f_l^{ij, \text{Ni}}(\omega) \equiv \langle t_l^n \rangle f_n^{ij} \Big|_{n=\text{Ni}} = s_l f_{2+}^{ij}(\omega) + p_l^{3+} f_{(2+)\rightarrow(3+)}^{ij}(\omega), \quad (4)$$

where $f_{2+}^{ij}(\omega)$ has the distribution of Ni cores $\{s_l\}$, to which spatially-dependent doping adds an additional term proportional to p_l^{3+} and $f_{(2+)\rightarrow(3+)}^{ij}(\omega)$. Therefore, the spatial symmetry of $f_l^{ij, \text{Ni}}(\omega)$ is determined not only by the distribution of Ni core states $\{s_l\}$, but also by the intermediate d -state through p_l^{3+} , the dopant distribution. The symmetry requiring the $L=2$ scattering to be small, noted in Sections II.A and II.E, is lifted in this way, by making the valences, and therefore the scattering factors, of Ni ions in outer and inner LNO layers different (Fig. 8b). This allows the $L=2$ reflection at the Ni edge. In contrast, because there is no change in the valence of the Cu ions (Section II.E), the Cu scattering factor $f_l^{ij, \text{Cu}}(\omega)$ depends on structure only, through $\{1 - s_l\}$, the complementary distribution to $\{s_l\}$, and the $L = 2$ reflection remains suppressed.

B. Ni valence modulation

We use this model to arrive at an estimate of the magnitude of Ni valence modulation in the LNO layers. Self-absorption is neglected because the calculated attenuation lengths are 1400 Å and 1600 Å at the Ni and Cu

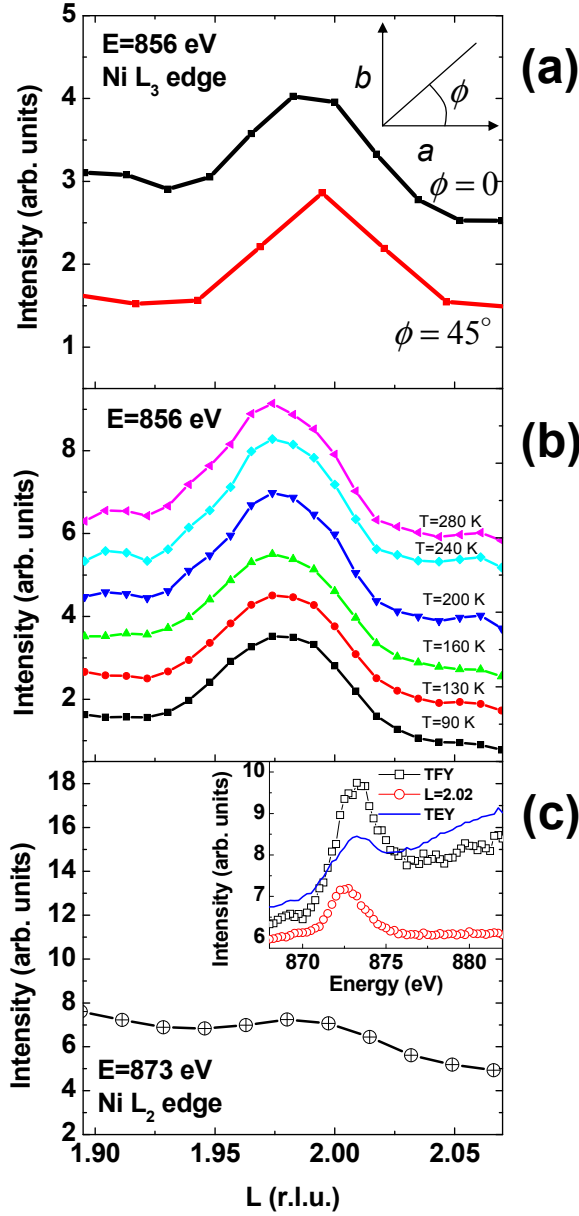


FIG. 7: (color online) (a) L scans at the Ni L_3 edge show the $L = 2$ peak for sample azimuthal orientations with incident beam polarization at 45° and along the tetragonal $a - b$ axes. (b) The $L = 2$ peak at the Ni L_3 edge persists up to at least 280 K. As will become clear in Section III.A, this is due to the larger energy necessary to move the oxygen dopants in the structure compared to the thermal energy needed to destroy a spin order. (c) The $L = 2$ peak at the Ni L_2 edge. The inset shows the energy profile of this peak (circles) compared to TFY (squares) and TEY (blue line).

edges, respectively, compared to the total SL thickness of 575 \AA , and the measured inverse momentum widths of the $L=1$ SL peaks, equal to $525 \pm 50 \text{ \AA}$ and $620 \pm 50 \text{ \AA}$ at the Ni and Cu edges respectively, are consistent with the total SL thickness of $575 \pm 20 \text{ \AA}$. In addition, self-absorption has a clear signature in FY in the form of

an increase in the intensity above the edge³¹, not seen in measurements on the LNO-LCO SL at the Cu edge (Fig. 6c). The slope in FY in Fig. 7c (inset) is due to a peak in the undulator spectrum. The relatively small self-absorption and the RSXS scattering geometry away from grazing incidence (the detector angles were 19.8° and 37.6° for $L=1$ and $L=2$ reflections at the Ni edge) support the use of a single-scattering model for the analysis of the RSXS measurements.

The contribution to scattering from, for instance, far-away resonances and the relatively small difference between the c -axis parameters of LNO and LCO is negligible because it would give a non-resonant energy intensity tail at $L=2$ near Ni edge, which is not observed (Fig. 6a). S_2 , the $L=2$ structure factor in Eq. 1, will then be proportional to $\Delta = |\sum_l p_l^{3+} e^{i4\pi z_l/c}|$, the $L=2$ component of the Fourier transform of the set $\{p_l^{3+}\}$.

In addition, S_2 will be proportional to $f_{(2+)\rightarrow(3+)}$, giving the energy variation of $L = 2$ scattering. However, the $L=2$ scattering is clearly made of only one peak (Figs. 7c and 8a) and the relatively small scattering angles suppress the scattering intensity from the doped $d_{x^2-y^2, \downarrow}$ states, which suggests that we can neglect this scattering channel. The contributions to scattering from terms proportional to f^{xx} and f^{yy} are suppressed at small scattering angles and the contribution from a small σ -polarized beam component is neglected. Then, the only terms left from Eqs. 2 and 3 are those proportional to $f_{d_{3z^2-r,2,\uparrow}}^{zz}$ and $f_{d_{3z^2-r,2,\downarrow}}^{zz}$.

The discussion in Sec. III A is independent of the specific details of the SL structure, given by the $\{s_L\}$ distribution. However, to obtain a numerical estimate, it is necessary to refer to the SL structure from our HXR measurements. The intensities of $L=2$ and $L=1$ scattering for an 8 ML superlattice at the Ni edge given by Eq. 1 are:

$$I(L=2)|_{Ni} = A_{L=2}(\Delta)^2 \left| \frac{f_{d_{3z^2-r,2,\downarrow}}^{zz}}{2} \right|^2 \cos^4(\theta_{L=2}) \quad (5)$$

$$I(L=1)|_{Ni} = A_{L=1}(2.61)^2 |f_{d_{3z^2-r,2,\uparrow}}^{zz}|^2 \cos^4(\theta_{L=1}) \quad (6)$$

where $|\sum_{l=1}^8 s_l e^{i2\pi z_l/c}| = |\sum_{l=1}^4 e^{i2\pi z_l/c}| = 2.61$ and the smaller contribution to S_1 proportional to Δ has been neglected. Using $f_{d_{3z^2-r,2,\downarrow}}^{zz} \approx f_{d_{3z^2-r,2,\uparrow}}^{zz}$ (from, for instance, the small XMLD for Ni^{2+} ions³²) and neglecting footprint effects ($A_{L=1} \approx A_{L=2}$), the ratio of $L=2$ to $L=1$ scattering intensity is:

$$\frac{I(L=2)}{I(L=1)} \Big|_{Ni} = \frac{(\frac{\Delta}{2})^2 \cos^4(\theta_{L=2})}{(2.61)^2 \cos^4(\theta_{L=1})}. \quad (7)$$

The scattering at $L=2$ is well separated in energy at the Ni and La edges (Fig. 6). However, this is not the case for $L=1$.³³ In practice, to obtain the value of the scattering intensity for $L=1$ at the Ni edge, we cut through the 2-dimensional profile at the energy where the $L=2$ scattering has the maximum intensity. This is justified by the

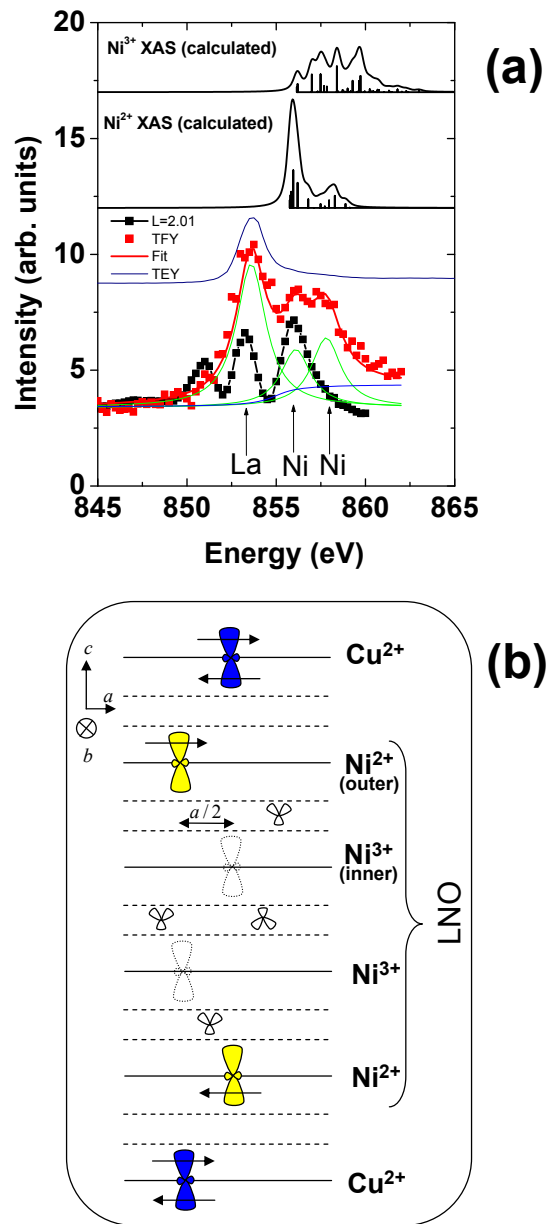


FIG. 8: (color online) (a) Calculated XAS (offset vertically for clarity) using the software “Missing”³⁰ for the Ni^{3+} and Ni^{2+} valences are in good agreement with Ref.²⁹. The parameters used were $10Dq = 1$ eV, $Ds = Dt = 0$, 0.8 Slater integrals scaling, 0.2 eV Lorentzian and 0.1 eV Gaussian broadenings. Instead of the full tetragonal D_{4h} symmetry, which further splits the final d -states, a cubic crystal field, with d -states of octahedral O_h symmetry, has been used for simplicity. The lower panel shows the measured electron yield (navy line), fluorescence yield (red squares) at La M_4 and Ni L_3 edges, and the fit of TFY (red line) with three peaks at the La and Ni edges (green) on a smooth step function (blue). The scattering at $L=2$ (black squares) peaks at the first Ni peak only. The lowest energy peak at 851 eV is a fringe effect, seen more clearly in Fig. 6a. (b) Sketch of the layer-resolved orbital occupation where, for clarity, a LNO layer with 4 ML has been illustrated and only the $d_{3z^2-r^2}$ orbitals have been included. Dashed lines represent the double LaO layers between which oxygen interstitials are located. Their number has been exaggerated in this sketch and the tri-lobe drawing (not to scale) illustrates their hybridization with La ions in the two adjacent LaO layers along axes at 90° with each other.¹⁵ A small spin gradient is also shown at the interface.

simple shape of the SL resonance profiles at the Ni edge. The small contribution from the La edge tail is neglected. From the measurements $\frac{I(L=2)}{I(L=1)} \Big|_{\text{Ni}} = 0.0185$, $\theta_{L=1} = 9.9^\circ$ and $\theta_{L=2} = 18.8^\circ$. Then, from Eq. 7, $\Delta = 0.77$, or a change in the average Ni ion valence between the inner and outer layers of $(p_{in}^{3+} - p_{out}^{3+}) = \Delta/\sqrt{2} = 0.54$.

The calculations above were made for an ideal superlattice, with no interfacial roughness. STEM^{34,35} and HXR measurements (e.g., in Ref. 5) have shown that interface mixing in complex oxide layers is well approximated by a Gaussian roughness. STEM measurements on the LNO-LCO SL (data not shown) are consistent with this assumption. We now consider a Gaussian intermixing distribution at the interfaces. Using as upper and lower limits the surface roughness $\sigma = 0.53$ nm (Section II.A) and $1/2$ ML, because of the mixing of 7 ML and 8 ML superperiods, we obtain an interface roughness $\sigma_i = 4.25 \pm 1$ Å. Including roughness effects in a scattering model suppresses the scattering intensity at $L = 2$ more than at $L = 1$ and increases the value for $(p_{in}^{3+} - p_{out}^{3+})$ calculated from the measurements. Specifically, Δ_R (with roughness included) is $\Delta_R = \sqrt{e^{3(2\pi\sigma_i/c)^2}} \Delta \approx 1.49\Delta$ and $(p_{in}^{3+} - p_{out}^{3+})_R = 0.8$.

HXR measurements showed that the superlattice is made of both 8 ML and 7 ML superperiods (Section II.A); a similar calculation as the above for a 7 ML superperiod gives $(p_{in}^{3+} - p_{out}^{3+})_R = 1.1$. The average of the two structures is 0.95. These calculations show a valence change of 50 – 100 %, pointing to a considerable modulation of the Ni valence between the inner and the outer LNO layers, much larger than that expected from chemical bonding of 1 – 10 %. The large valence change is possible in our case because of the high doping of the LNO layers with interstitial oxygen. Choosing a larger valence for Ni ions inside the LNO layers is justified by the oxygen affinity of LNO; the Ni $d_{3z^2-r^2}$ and $d_{x^2-y^2}$ orbitals are emptied preferentially away from the interfaces. The case of a valence change of 1 is represented schematically in Fig. 8b.

The layer scattering factor was obtained above by interpolating between nominal Ni^{2+} and Ni^{3+} form factors statistically with weights $\{p_l\}$. The same results obtain for a scattering model describing a fractional valence common to all Ni ions in a NiO_2 layer, in which a linear dependence of the Ni ion form factor on doping for intermediate valences between Ni^{2+} and Ni^{3+} is used. Which model better represents the reality depends on whether the oxygen interstitials dope only the immediate Ni neighbor ions or a large number of ions in the NiO_2 layers. Our experiment cannot distinguish between these two cases.

The large Ni valence modulation would suggest a similar effect in the valence of the oxygen ions, in addition to their layer-dependent density shown in Fig. 8b. One possible indication of this effect is the feature seen at 533.5 eV (Fig. 5). It is a state in the LNO layers since it aligns with a peak in TEY spectrum (Fig. 4). In contrast to the

LNO MCP state, it has a large intensity at $L = 2$, similar to the Ni edge scattering. It has also been observed for very high doping in the $\text{La}_{2-x}\text{Sr}_x\text{CuO}_4$ system, which has no interstitial oxygen.³⁶ This suggests that it is an apical oxygen state hybridized with Ni orbitals, responding to the large Ni valence modulation.

IV. CONCLUSION

We observed a non-uniform distribution of holes in a LNO-LCO superlattice, with doped LNO layers and essentially undoped LCO layers. As for bulk LCO and LNO, the holes in the LCO layers are oriented in the $a - b$ plane, while the holes in the LNO layers have a substantial c -axis component. The difference in the hole affinities of LCO and LNO layers modulates the valence and the orbital occupation of the Ni ions in the LNO layers, with the Ni $d_{x^2-y^2, \downarrow}$ and $d_{3z^2-r^2, \downarrow}$ orbital states preferentially occupied near the interfaces. Since the density of oxygen interstitials can be continuously modified with standard techniques, the Ni orbital occupation near the interfaces in 214 LNO-LCO superlattices is tunable. In contrast to the ferromagnetism of this structure, this orbital occupation is more robust, being stable up to at

least 280 K.

It would be useful to explore combinations of 214 oxides (manganites, titanates, etc.) in which the orbital occupations near the interfaces can be changed by selective oxygen doping so as to leave only one orbital unoccupied, similar to superconducting cuprates. For superconducting samples it might be desirable to avoid ferromagnetism. On the other hand, it would be interesting to investigate 214 systems with magnetic orders with uncompensated spins at interfaces, for instance A-type antiferromagnets, for which the magnetic interactions across interfaces are sufficiently strong to correlate the spins and create a magnetically active interface.^{37,38}

V. ACKNOWLEDGMENTS

We thank A. Gozar for useful discussions. This work was supported by the Department of Energy: RSXS measurements by grant DE-FG02-06ER46285, superlattice growth by MA-509-MACA, National Synchrotron Light Source by DE-AC02-98CH10886, Materials Research Laboratory facilities by DE-FG02-07ER46453 and DE-FG02-07ER46471, and Advanced Photon Source by DE-AC02-06CH11357.

* Present address: Max-Planck-Institut, Festkörperforschung, 70569, Stuttgart, Germany.

¹ J. Chakhalian, J. W. Freeland, H.-U. Habermeier, G. Cristiani, G. Khaliullin, M. van Veenendaal, and B. Keimer, *Science* **318**, 1114 (2007).

² J. Chakhalian, J.W. Freeland, G. Srajer, J. Strempfer, G. Khaliullin, J.C. Cezar, T. Charlton, R. Dalgliesh, C. Bernhard, G. Cristiani, H.U. Habermeier, and B. Keimer, *Nature Physics* **2**, 244 (2006).

³ J. Chaloupka and G. Khaliullin, *Physical Review Letters* **100**, 016404 (2008).

⁴ P. Hansmann, X. Yang, A. Toschi, G. Khaliullin, O. K. Andersen, and K. Held, *Physical Review Letters* **103**, 016401 (2009).

⁵ E. Benckiser, M.W. Haverkort, S. Brück, E. Goering, S. Macke, A. Frañó, X. Yang, O.K. Andersen, G. Cristiani, H-U. Habermeier, A.V. Boris, I. Zegkinoglou, P. Wochner, H-J. Kim, V. Hinkov, and B. Keimer, *Nature Materials* **10**, 189 (2011).

⁶ A. V. Boris, Y. Matiks, E. Benckiser, A. Frano, P. Popovich, V. Hinkov, P. Wochner, M. Castro-Colin, E. De-temple, V. K. Malik, C. Bernhard, T. Prokscha, A. Suter, Z. Salman, E. Morenzoni, G. Cristiani, H.-U. Habermeier, B. Keimer, *Science* **332**, 937 (2011).

⁷ B.R.K. Nanda and S. Satpathy, *Physical Review B* **78**, 054427 (2008).

⁸ G. Herranz, M. Basletic, M. Bibes, C. Carretero, E. Taffra, E. Jacquet, K. Bouzouhane, C. Deranlot, A. Hamzic, J.-M. Broto, A. Barthelemy, and A. Fert, *Physical Review Letters* **98**, 216803 (2007).

⁹ S. Smadici, J. C. T. Lee, S. Wang, P. Abbamonte, G. Logvenov, A. Gozar, C. Deville Cavellin, and I. Bozovic,

Physical Review Letters **102**, 107004 (2009).

¹⁰ J.M. Tranquada, Y. Kong, J. E. Lorenzo, D. J. Buttrey, D. E. Rice, and V. Sachan, *Physical Review B* **50**, 6340 (1994).

¹¹ G. Shirane, Y. Endoh, R.J. Birgeneau, M.A. Kastner, Y. Hidaka, M. Oda, M. Suzuki, and T. Murakami, *Physical Review Letters* **59**, 1613 (1987).

¹² A. Demourgues, P. Dordor, J.-P. Doumerc, J.-C. Grenier, E. Marquestaut, M. Pouchard, A. Villesuzanne, and A. Wattiaux, *J. Solid State Chemistry* **124**, 199 (1996).

¹³ K. Yamada, T. Ornata, K. Nakajima, S. Hosoya, T. Sumida, and Y. Endoh, *Physica C* **191**, 15 (1992).

¹⁴ M. Fujita, K. Yamada, H. Hiraka, P.M. Gehring, S.H. Lee, S. Wakimoto, and G. Shirane, *Phys. Rev. B* **65**, 064505 (2002).

¹⁵ J.D. Jorgensen, B. Dabrowski, S. Pei, D.R. Richards, and D.G. Hinks, *Physical Review B* **40**, 2187 (1989).

¹⁶ E. Pellegrin, J. Zaanen, H.-J. Lin, G. Meigs, C. T. Chen, G. H. Ho, H. Eisaki, and S. Uchida, *Physical Review B* **53**, 10667 (1996).

¹⁷ P. Kuiper, J. van Elp, G.A. Sawatzky, A. Fujimori, S. Hosoya, and D.M. de Leeuw, *Physical Review B* **44**, 4570 (1991).

¹⁸ C.T. Chen, F. Sette, Y. Ma, M.S. Hybertsen, E.B. Stechel, W. M. C. Foulkes, M. Schluter, S-W. Cheong, A. S. Cooper, L. W. Rupp, Jr., B. Batlogg, Y. L. Soo, Z. H. Ming, A. Krol, and Y.H. Kao, *Physical Review Letters* **66**, 104 (1991).

¹⁹ P. Abbamonte, *Physical Review B* **74**, 195113 (2006).

²⁰ P. Abbamonte, A. Ruydi, S. Smadici, G.D. Gu, G.A. Sawatzky, and D.L. Feng, *Nature Physics* **1**, 155-158 (2005).

- ²¹ P. Abbamonte, G. Blumberg, A. Rusydi, A. Gozar, P.G. Evans, T. Siegrist, L. Venema, H. Eisaki, E. D. Isaacs, and G.A. Sawatzky, *Nature* **431**, 1078 (2004).
- ²² P. Abbamonte, L. Venema, A. Rusydi, G.A. Sawatzky, G. Logvenov, I. Bozovic, *Science* **297**, 581 (2002).
- ²³ S. Smadici, P. Abbamonte, A. Bhattacharya, X. Zhai, B. Jiang, A. Rusydi, J.N. Eckstein, S.D. Bader, and J-M. Zuo, *Physical Review Letters* **99**, 196404 (2007).
- ²⁴ P. Kuiper, D.E. Rice, D.J. Buttrey, H.-J. Lin, and C.T. Chen, *Physica B* **208**, 271 (1995).
- ²⁵ J. Zaanen, G.A. Sawatzky, and J.W. Allen, *Physical Review Letters* **55**, 418 (1985).
- ²⁶ C. T. Chen, L. H. Tjeng, J. Kwo, H. L. Kao, P. Rudolf, F. Sette, and R. M. Fleming, *Physical Review Letters* **68**, 2543 (1992).
- ²⁷ P. Kuiper, J. van Elp, D.E. Rice, D.J. Buttrey, H.-J. Lin, and C. T. Chen, *Physical Review B* **57**, 1552 (1998).
- ²⁸ S. Yamamoto, T. Fujiwara, and Y. Hatsugai, *Physical Review B* **76**, 165114 (2007).
- ²⁹ F.M.F. de Groot, J.C. Fuggle, B.T. Thole, G.A. Sawatzky, *Physical Review B* **42**, 5459 (1990).
- ³⁰ <http://www.esrf.eu/computing/scientific/MISSING/>.
- ³¹ S. Eisebitt, T. Böske, J.-E. Rubensson, and W. Eberhardt, *Physical Review B* **47**, 14103 (1993).
- ³² E. Arenholz, G. van der Laan, R.V. Chopdekar, and Y. Suzuki, *Physical Review Letters* **98**, 197201 (2007).
- ³³ See Supplemental Material at [URL will be inserted by publisher] for the scattering intensity at the La $M_{5,4}$ and Ni $L_{3,2}$ edges near $L=1$.
- ³⁴ A. Ohtomo, D.A. Muller, J.L. Grazul and H.Y. Hwang, *Nature* **419**, 378 (2002).
- ³⁵ D.R. Hamann, D.A. Muller, and H.Y. Hwang, *Physical Review B* **73**, 195403 (2006).
- ³⁶ S. Smadici *et al.*, manuscript in preparation.
- ³⁷ J. Freeland, K.E. Gray, L. Ozyuzer, P. Berghuis, E. Badica, J. Kavich, H. Zheng, J.F. Mitchell, *Nature Materials* **4**, 62 (2005).
- ³⁸ D. Coffey, T.M. Rice, and F.C. Zhang, *Physical Review B* **44**, 10112 (1991).